Ocean Dynamics (2002) 52: 104–115
DOI 10.1007/s10236-002-0012-9

William D. Smyth · Eric D. Skyllingstad
Gregory B. Crawford · Hemantha Wijesekera

Nonlocal fluxes and Stokes drift effects in the K-profile parameterization

Received: 31 August 2001 / Accepted: 15 December 2001

Abstract The K-profile parameterization of upper-ocean mixing is tested and extended using observations and large eddy simulations of upper-ocean response to a westerly windburst. A nonlocal momentum flux term is added, and the amplitude of the nonlocal scalar flux is recalibrated. Parameterizations of Stokes drift effects are added following recent work by McWilliams and Sullivan (2001). These changes allow the parameterization to produce both realistic gradients of momentum and scalars in the nocturnal boundary layer and enhanced mixing during stable conditions. The revised parameterization is expected to produce improved representations of lateral advection and sea-surface temperature in large-scale models.

Keywords Ocean modeling · Turbulence · Mixed layer · K-profile parameterization · KPP

1 Introduction

A central goal of ocean turbulence research is the development of efficient, accurate parameterizations of vertical mixing for use in large-scale models. Currently popular approaches include the Mellor–Yamada hierarchy of models (e.g., Mellor and Yamada 1982; Kantha and Clayson 1994), the k–ϵ model (e.g., Burchard et al. 1998) and the nonlocal K-profile parameterization (KPP), introduced by Large et al. (1994). Every mixing parameterization represents a compromise between accuracy and efficiency. Of the currently popular models, the KPP is the most efficient; it forsakes theoretical development almost entirely in favor of simple, empirical representations of specific processes. The result is a scheme that involves no evolution equations and is therefore extremely cheap in terms of computer cycles and memory. In contrast, more accurate schemes such as the k–ϵ model require storage and transport operations for two turbulence quantities in addition to the usual hydrodynamic field variables. Computational efficiency is crucial in large-scale models, where the need to resolve mesoscale eddies puts extreme demands on computer capacity. Since its introduction, the KPP has undergone significant refinement (e.g., Large and Gent 1999; McWilliams and Sullivan 2001), in terms of both adding new processes to the model and refining the empirical constants that quantify those processes. Here, we further this effort via comparisons with both observations and large eddy simulations (LES) of upper-ocean structure during a westerly windburst in the equatorial Pacific Ocean. Of particular interest to us are “nonlocal” vertical property fluxes and Stokes drift effects. Nonlocal fluxes are driven by eddies on scales comparable to or larger than the vertical scale over which the background shear and stratification change. In the nocturnal boundary layer, for example, net surface cooling generates a mean density gradient which is unstable near the surface, nearly zero within the mixed layer, and strongly stable in the entrainment zone at the base of the mixed layer. Convective plumes carry property fluxes that depend on the net buoyancy change across the mixed layer, and therefore have little relationship to the local gradient at any particular depth. Such fluxes can be strong even in the mixed layer interior, where the background gradients are near zero. Parameterization of these fluxes using the standard gradient-diffusion formalism is clearly inappropriate.

Improper representation of nonlocal fluxes promotes excessively strong vertical gradients within the mixed layer, as we will show. This consequence is not

Responsible Editor: Hans Burchard

W. D. Smyth (✉) · E. D. Skyllingstad · H. Wijesekera
College of Oceanic and Atmospheric Sciences,
Oregon State University, Corvallis, Oregon 97331-5503, USA
e-mail: smyth@coas.oregonstate.edu

G. B. Crawford
Department of Oceanography, Humboldt State University,
Arcata, California 95521-8299, USA

the worst that could be envisioned, as it allows the net property fluxes across the boundary layer to be represented with reasonable accuracy. Nevertheless, the deficiency is potentially serious. For example, excessive shear in the mixed layer leads to unrealistic lateral advection in a large-scale model. Unrealistic values for surface currents can lead to major errors in regions with strong fronts, such as coastal boundaries and near western boundary currents (e.g., the Gulf Stream), and any region of the ocean with strong wind-driven circulations (e.g., coastal upwelling). Increased mixing of momentum by nonlocal fluxes can also alter the entrainment rate at the mixed layer base, thereby changing the bulk characteristics of the upper ocean.

The meteorological community has studied nonlocal fluxes in the atmospheric boundary layer (ABL) extensively (e.g., Deardorff 1972; Mailhot and Benoit 1982; Therry and Lacarrere 1983; Troen and Mahrt 1986; Holtzag and Moeng 1991; Frech and Mahrt 1995; Brown and Grant 1997), and has developed useful formalisms for their incorporation into atmospheric models. Large et al. (1994) took advantage of the similarity between the ABL and the upper ocean boundary layer (OBL) to bring meteorological experience to bear on the ocean problem, and thereby provided for the inclusion of nonlocal fluxes in the KPP. At present, this effort is far from complete. While useful mathematical representations for nonlocal fluxes have been developed, sensitivity experiments are needed to establish proper values for the adjustable parameters. Even in the atmospheric context there have been few such studies, and the possibility that different parameter values may be needed for the ocean case has not been addressed at all.

Here, we describe a study of turbulent fluxes in the upper equatorial ocean during a westerly windburst. This is a suitable regime for the quantification of nonlocal transports as it involves both vigorous convection and strong surface fluxes of heat, salt, and momentum. We take advantage of the extensive and detailed observational database that resulted from TOGA-COARE (Webster and Lukas 1992; Moum and Caldwell 1994; Smyth et al. 1996a,b). Skyllingstad et al. (1999) described large-eddy simulations (LES) of upper-ocean mixing over a 24-h period during a windburst using a model initialized with observed mean profiles and driven by observed surface fluxes. Statistical comparisons quantified the relationship between turbulent fluxes developed in the LES model and those inferred from in situ microstructure measurements. These comparisons establish the accuracy (and limits thereto) of the LES description of upper-ocean turbulence, which is much more comprehensive than the view that the observations afford. Modeled turbulence statistics were shown to compare closely with observations in the mixed-layer interior. Model performance was poorer in the stratified region below the mixed layer, wherein the energy-containing scales of the turbulence contract to values smaller than the model's spatial resolution.

Our plan here is to test the performance of the KPP model in this oceanic regime and suggest appropriate refinements. For this purpose, the KPP is incorporated into a one-dimensional model of the upper ocean, which is then initialized and forced using observations in the same manner as is the LES. Besides testing the KPP as a model for mixing in the windburst regime, we will derive values for the adjustable parameters needed to describe nonlocal fluxes of heat, salt, and momentum in the upper ocean. In addition, we investigate two modifications to the KPP model that account for the effects of the Stokes drift, following suggestions of McWilliams and Sullivan (2001). First, the turbulent velocity scale is enhanced during stable conditions to account for fluxes due to Langmuir cells. Second, the nonlocal momentum flux is supplemented by a term describing mixing of the Stokes drift velocity gradient.

We begin in Section 2 with a discussion of our methodology. The LES methods and observational measurements are reviewed briefly, as is the overall structure of the KPP. Greater attention is given to methods for the parameterization of nonlocal fluxes and to the inclusion of penetrating solar radiation. Preliminary comparisons among observations, LES results, and results from the column model are described in Section 4. These comparisons guide the more detailed analyses discussed later. Section 5 describes the essential results of the paper: modifications to the KPP that account for Stokes drift effects as well as revisions to the nonlocal flux parameterizations. Our main conclusions are summarized in Section 6.

2 Observations

The R/V Moana Wave maintained station at 1°45′S, 156°0′E from December 20th, 1992, to January 12th, 1993. Onboard meteorological measurements were processed using the TOGA-COARE bulk flux algorithm (Fairall et al. 1996) to yield surface fluxes. Currents were measured using the shipboard Acoustic Doppler Current Profiler in combination with data from a nearby mooring (Weller and Anderson 1996). Temperature, conductivity, and shear microstructure were measured using the Chameleon microstructure profiler (Moum et al. 1995).

The 24-h period selected for analysis began at 00:00 h UTC on December 31st, 1992. This period began in local midafternoon. Cloud cover was minimal, and winds were strong and steady from the west (Fig. 1a). A squall at $t = 2$ h interrupted the surface warming. The evening reversal of the surface heat flux led to convective conditions in the upper-ocean and a rapid deepening of the mixed layer (Fig. 1b). Upper-ocean current structure was dominated by the wave response to the windburst and by the semidiurnal tide (Smyth et al. 1996a). Thermal evolution during this

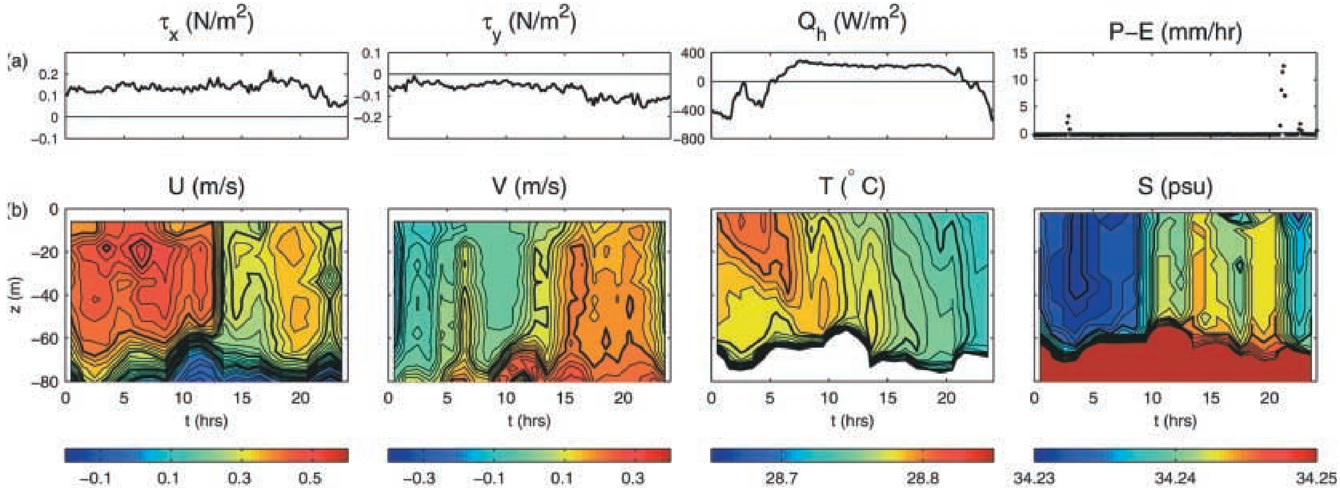

Fig. 1a, b COARE observations. **a** Wind stresses, net surface heat flux, and net precipitation rate observed at 156 E, −1.75 S for the 24-h period beginning on day 366 of 1992. **b** Time–depth sections of zonal current, meridional current, temperature, and salinity

period was controlled mainly by the local surface heat flux, while salinity increased in response to advection (Smyth et al. 1996b; Feng et al. 1998). The morning reversal of the heat flux was delayed by a second rain squall. Rain effects during this period are described more fully in Smyth et al. (1997).

Note that, despite complex time dependence, the velocity and salinity fields (shown in the first, second, and fourth frames of Fig. 1b) are dominated by nearly vertical isolines in the upper 60 m, suggesting that these fields are generally well mixed in this near-surface regime. The temperature field (third frame of Fig. 1b) exhibits stable stratification during the first few hours of the observation (the daytime portion), consistent with solar heating. Once the evening deepening of the mixed layer is complete, the temperature stratification in the upper 60 m is reversed, with the highest temperatures occurring at around 50–60 m depth and colder water evident at the surface, as is typical in strongly convective conditions (e.g., Anis and Moum 1992).

3 Models

3.1 The LES model

Our large-eddy modeling methods are described in detail in Skyllingstad et al. (1999, 2000), and thus will be only summarized here. The computational domain is a 96-m-deep layer adjacent to the ocean surface, with lateral size 384×384 m. The domain is periodic in both lateral directions. A radiation boundary condition is applied at the model bottom, and surface fluxes provide the upper boundary conditions. Surface wave effects are incorporated using the Stokes vortex force, with wave parameters based on observations. Subgrid scale (SGS) fluxes are parameterized using the filtered structure function method of Ducros et al. (1996). Spatial derivatives are discretized using second-order finite differences in flux form on a staggered C-grid, with spacing 1.5 m in all three coordinates. Time stepping is via the third-order Adams–Bashforth method. As in Skyllingstad et al. (1999), the simulation was initialized using measured profiles of velocity, temperature, and salinity, and forced subsequently by the observed surface fluxes described above. Simulations described here were performed on a 32 processor IBM SP-3.

3.2 The column model

The column model employed here solves the following equations for the zonal velocity $U(z,t)$, the meridional velocity $V(z,t)$, the temperature $T(z,t)$ and the salinity $S(z,t)$:

$$\frac{\partial U}{\partial t} = -\frac{\partial}{\partial z}\overline{u'w'} + fV \quad ; \tag{1}$$

$$\frac{\partial V}{\partial t} = -\frac{\partial}{\partial z}\overline{v'w'} - fU \quad ; \tag{2}$$

$$\frac{\partial T}{\partial t} = -\frac{\partial}{\partial z}\overline{T'w'} - \frac{1}{\rho_o C_p}\frac{\partial Q_r}{\partial z} \quad ; \tag{3}$$

$$\frac{\partial S}{\partial t} = -\frac{\partial}{\partial z}\overline{S'w'} \quad , \tag{4}$$

where z and t represent the vertical coordinate and time, respectively, f is the Coriolis parameter, and $Q_r(z,t)$ is a specified function representing the radiative heat flux. The mean density is approximated by $\rho_o = 1030\,\mathrm{kgm}^{-3}$, and the specific heat capacity of water is $C_p = 4000\ \mathrm{Jkg}^{-1}\mathrm{K}^{-1}$. The fluxes $\overline{x'w'}(z,t)$ (where x stands for any of u, v, T, and S and primes represent turbulent fluctuations) are determined using the nonlocal K-profile parameterization described below. Initial conditions are provided by specified functions $U(z,0)$, $V(z,0)$, $T(z,0)$, and $S(z,0)$. Time-dependent values of the surface fluxes $\overline{x'w'}(0,t)$ are specified, while all fluxes are assumed to vanish at the lower domain boundary: $\overline{x'w'}(-D,t) = 0$.

In the present application, the initial profiles and the fluxes at the upper boundary are provided by observational data and are identical to those used in the LES (Sect. 3.1).

The vertical discretization is staggered, with fluxes being computed at a set of equally spaced depths that include the upper and lower boundaries, and all prognostic variables defined on the intermediate points. Vertical derivatives are represented as second-order centered differences. The local components of the fluxes (see below) are advanced implicitly using the second-order Crank–Nicolson scheme, as is the radiative heat flux. The nonlocal fluxes, as well as the Coriolis terms, are advanced explicitly using the second-order Adams–Bashforth method.

The parameterization for the turbulent fluxes that appear in Eqs. (1–4) has been described in detail by Large et al. (1994). Here, we summarize the features that are most pertinent to the present experiments and describe the addition of the nonlocal momentum fluxes and Stokes drift effects. The parameterization requires separating the water column into two regions, the boundary layer and the underlying thermocline, which are separated by the surface $z = -h(t)$. The boundary layer depth $h(t)$ is defined as the shallowest depth at which the bulk Richardson number, $\mathrm{Ri}_b(z,t)$, exceeds a specified critical value Ri_c. The bulk Richardson number is defined by

$$\mathrm{Ri}_b = \frac{B_{sl} - B}{\left|\vec{U}_{sl} - \vec{U}\right|^2 + V_t^2}(z_{sl} - z) \tag{5}$$

The buoyancy $B(z,t)$ is given by $-g\rho(z,t)/\rho_o$, where $g = 9.81\,\mathrm{ms}^{-2}$ is the gravitational acceleration and $\rho(z,t)$ is the density (obtained as a function of T and S using a standard equation of state for seawater). $\vec{U}(z,t)$ is the horizontal velocity vector (U, V). The subscript sl indicates values averaged over the surface layer, which is taken to be the upper one-tenth of the boundary layer, i.e., $-0.1\,h < z < 0$. In practice, the surface-layer depth is computed using an initial guess at h, usually obtained as the value at the previous time step. The computation may be iterated if the time step is too large to resolve fluctuations in boundary-layer depth accurately. In the present application, iteration is not required. V_t is a turbulent velocity magnitude described in detail in Large et al. (1994) (their Eq. 23). We will not repeat Large et al's description except to note that V_t^2 is proportional to a constant parameter C_v, whose value will be of interest to us here.

Each of the fluxes $\overline{x'w'}$ that appears in Eqs. (1–4) is expressed as a local and a nonlocal part, viz:

$$\overline{x'w'} = \overline{x'w'}_L + \overline{x'w'}_N \quad . \tag{6}$$

The local component is given by the usual gradient parameterization

$$\overline{x'w'}_L = -K_x \frac{\partial X}{\partial z} \quad , \tag{7}$$

where $K_x(z,t)$ is the turbulent diffusivity and $X(z,t)$ represents any of U, V, T, and S. Parameterization of K_x is discussed in the remainder of this subsection; nonlocal fluxes are discussed in detail in Sect. 3.3.

Below the boundary layer $(z < -h)$, fluxes are entirely local and are defined using a simple parameterization based on the gradient Richardson number, $\mathrm{Ri} = \frac{\partial B}{\partial z}/|\frac{\partial \vec{U}}{\partial z}|^2$, viz:

$$K_x = \nu_x^w + \nu^o \begin{cases} 1 & \mathrm{Ri} < 0 \\ (1 - \mathrm{Ri}^2/\mathrm{Ri}_0^2)^3 & 0 < \mathrm{Ri} < \mathrm{Ri}_0 \\ 0 & \mathrm{Ri} > \mathrm{Ri}_0 \end{cases} . \tag{8}$$

The first term approximates diffusivity due to internal wave breaking, and takes the constant values $\nu_m^w = 1.0 \times 10^{-4}\mathrm{m}^2\mathrm{s}^{-1}$ for momentum and $\nu_s^w = 1.0\times 10^{-5}\mathrm{m}^2\mathrm{s}^{-1}$ for scalars. The second term parameterizes diffusivity due to shear instability in regions of low Ri. The constant ν^0 has the value $5 \times 10^{-3}\mathrm{m}^2\mathrm{s}^{-1}$. The cutoff value for the gradient Richardson number, Ri_0, was set to 0.7 by Large et al. (1994). Large and Gent (1999) suggested that Ri_0 be increased to 0.8. However, results presented here motivate retention of the smaller value.

Within the boundary layer $(z > -h)$, the diffusivity K_x is parameterized by

$$K_x(z,t) = h(t)w_x(z,t)G_x(z,t) \quad , \tag{9}$$

in which w_x is a turbulent velocity scale and G_x is a shape function. The velocity scales are given by

$$w_x(z,t) = \frac{\kappa u_*(t)}{\phi_x(z,t)} \quad , \tag{10}$$

where $\kappa = 0.4$ is the von Karman constant and u_* is the surface friction velocity. The structure function ϕ_x is defined as a function of the scaled depth $\zeta = z/L$, where L is the Monin–Obukhov length scale (see Large et al. (1994) Eqs. B1 and B2 for details). Continuity of fluxes requires that near-surface gradients obey the similarity scaling

$$\frac{\partial X}{\partial z} = -\frac{\overline{x'w'}_0}{u_*}\frac{\phi_x(\zeta)}{\kappa|z|} \quad , \tag{11}$$

where $\overline{x'w'}_0$ is the surface flux of x (positive upwards). In unstable conditions, ϕ is restricted so that it cannot exceed its value at the base of the surface layer. The shape function G_x is a cubic polynomial in ζ whose four coefficients are determined by four matching conditions: at the surface $G_x = 0$ and $\partial G_x/\partial\zeta = 1$, and at $z = -h$ both the diffusivity K_x and its first derivative must be continuous with the values determined below the boundary layer by the Richardson number parameterization.

McWilliams and Sullivan (2001) have suggested that extra mixing due to Langmuir circulations be accounted for by multiplying the turbulent velocity scale w_x by a factor $(1 + C_w/\mathrm{La}^4)^{1/2}$, where La is the Langmuir number, given by $\mathrm{La} = (u_*/U_s)^{1/2}$, and U_s is the Stokes drift velocity. This adjustment of the KPP model results in turbulent velocities proportional to U_s in the regime of small La, a known property of Langmuir turbulence. The constant C_w was given the value 0.08 on the basis of fits to large eddy simulations of quasistationary, weakly convecting Langmuir turbulence. McWilliams and Sullivan (2001) also suggested that this parameterization may require modification in regimes of either strong convection or strong wind forcing, both of which occur here. Accordingly, we multiply C_w by an additional factor that enhances the effect of Langmuir cells in stable (wind-forced) conditions and reduces it in convective conditions:

$$w_x(z,t) = \frac{\kappa u_*(t)}{\phi_x(z,t)} \times \left\{1 + \frac{C_w(u_*, w_*)}{La^4}\right\}^{1/2} , \tag{12}$$

in which

$$C_w(u_*, w_*) = C_{wo}\left[\frac{u_*^3}{u_*^3 + 0.6w_*^3}\right]^l , \tag{13}$$

w_* is the convective velocity scale (defined following Large et al. 1994 as $w_*^3 = \kappa B_f h$, where B_f is the surface bouyancy flux), and C_{wo} and l are constants to be determined.

3.3 Nonlocal fluxes in the KPP

The nonlocal flux of the property x is the flux due to eddies comparable in size to the scale on which the background gradient $\partial X/\partial z$ varies. Nonlocal fluxes may be written in terms of local variables by making various approximations to the flux budget (e.g., Deardorff 1972, Therry and Lacarrere 1983, Holtzag and Moeng 1991). In low-order closure models, however, those fluxes must be parameterized in terms of resolved variables. Typically, the parameterization is contained within an effective "gradient", $-\gamma_x(z,t)$, that is added to the background gradient, i.e.,

$$\overline{x'w'}_N = K_x\gamma_x . \tag{14}$$

Large et al. (1994) deferred the implementation of nonlocal momentum fluxes due to lack of observational data for calibration, and instead concentrated on parameterizing nonlocal scalar fluxes via the effective gradient γ_s. They set γ_s to zero in stable conditions, but for convective conditions used the definition

$$\gamma_s(z,t) = C_s\frac{\overline{s'w'}_0(t)}{w_s(z,t)h(t)} , \tag{15}$$

where s represents any scalar concentration, $\overline{s'w'}_0$ is the surface flux of s, and w_s is the turbulent velocity scale for scalars. The constant C_s is written as $C_s^*\kappa(c_s\kappa\epsilon)^{1/3}$, in which c_s is an additional constant that appears in the structure function for convective conditions: $\phi_s = (a_s - c_s\zeta)^{-1/3}$. C_s^* is regarded as a universal constant. The constant ϵ represents the depth of the surface layer as a fraction of the boundary layer depth, here equal to 0.1. In the original analyses of Deardorff (e.g., Deardorff 1972), the constant C_s^* was expected to be of order 10. Mailhot and Benoit (1982) adopted this value for their atmospheric simulations and obtained acceptable results. An explicit attempt to determine the best value for C_s^* was carried out by Therry and Lacarrere (1983), who obtained optimal results using the value $C_s^* = 5$. The same result was found by Holtzag and Moeng (1991) on the basis of comparisons with LES. In constructing the original KPP, Large et al. (1994) used Deardorff's estimate, $C_s^* = 10$. Results described later in this paper suggest that the smaller value is preferable.

A similar parameterization can be devised for the nonlocal momentum flux. Following the atmospheric modeling work of Brown and Grant (1997) and Frech and Mahrt (1995), we write

$$\gamma_{\vec{u}}(z,t) = -C_m\frac{u_*^2}{w_m(z,t)h(t)}A(u_*, w_*)\hat{\boldsymbol{e}} . \tag{16}$$

The constant C_m corresponds to S_m in Brown and Grant (1997) and Frech and Mahrt (1995), and is scaled as $C_m^*\kappa(c_m\kappa\epsilon)^{1/3}$ analogously with the scalar case. The factor $A(u_*, w_*)$ represents enhancement of the nonlocal flux in strongly unstable conditions. The unit vector $\hat{\boldsymbol{e}}$ defines the lateral direction of the flux.

Frech and Mahrt (1995) suggested that the stability function $A(u_*, w_*)$ takes the form

$$A(u_*, w_*) = 1 + w_*/u_* . \tag{17}$$

In more recent atmospheric simulations, Brown and Grant (1997) have shown that this form exaggerates the nonlocal flux in neutral stratification, and suggested the alternative form

$$A(u_*, w_*) = 2.7w_*^3/(u_*^3 + 0.6w_*^3) . \tag{18}$$

In our simulations of turbulence in the equatorial ocean, the expressions (17) and (18) for A are nearly proportional throughout the night (the second exceeds the first by a factor that varies between 1.22 and 1.25). However, A as defined by Eq. (18) vanishes during the day, a desirable property. We therefore adopt Eq. (18) as the stability function in the present work.

There is also uncertainty over the best representation of the direction vector, $\hat{\boldsymbol{e}}$. Frech and Mahrt (1995) defined $\hat{\boldsymbol{e}}$ as the direction of the mean vertical shear of the horizontal current between the middle of the surface layer and the base of the boundary layer, i.e., $\hat{\boldsymbol{e}} = (\vec{U}_{sl} - \vec{U}_h)/|\vec{U}_{sl} - \vec{U}_h|$. An alternative recommended by Brown and Grant (1997) is to have $\hat{\boldsymbol{e}}$ correspond to the direction of the wind. In the present equatorial regime, the Coriolis force is weak, so that the surface current remains nearly aligned with the wind. As a result, these two directions differ very little (by 10° or less during the night, when the nonlocal fluxes are active). For the present simulations, we retain the Brown and Grant definition.

A value must be chosen for the amplitude parameter, C_m or, equivalently, for C_m^*. Due to the lack of available data, Large et al. (1994) set C_m^* to zero. In comparisons of atmospheric boundary layer simulations with observations, Brown and Grant (1997) concluded that values of C_m up to 1.4 give reasonable results, while the preferred value is 0.8. In our notation, $C_m = 0.8$ and 1.4 correspond to $C_m^* = 2.3$ and 4.0, respectively.

Thus, available values for both C_m^* and C_s^* are based on atmospheric cases. A goal of the present paper is to provide values for these constants that are appropriate for the upper-ocean boundary layer (Sects. 5.2 and 5.3). Finally, McWilliams and Sullivan (2001) suggest that nonlocal momentum fluxes due to Langmuir cells be included in the model by adding the shear of the Stokes drift to γ_x. We will test that possibility in the present analyses (Sect. 5.4).

3.4 The radiative heat flux

Heat balances in the upper ocean during COARE were strongly influenced by the heat flux due to the penetration of solar radiation to significant depths beneath the sea surface (Weller and Anderson 1996, Smyth et al. 1996b, Ohlmann et al. 1998). Here, we parameterize the radiative heat flux as

$$Q_r(z,t) = E_d(t)Tr(z,t) \ , \tag{19}$$

in which E_d is the downwelling radiation measured just above the sea surface and Tr is the transmission function. $E_d(t)$ was measured locally (Fairall et al. 1996), and the transmission function was measured aboard a nearby vessel (Siegel et al. 1995, Ohlmann et al. 1998). Measured profiles of $Tr(z,t)$ were fitted to a two-term exponential decay representation:

$$Tr = r_1 e^{z/\mu_1} + r_2 e^{z/\mu_2} \tag{20}$$

using a nonlinear least-squares method (Fig. 2). [A four-term expansion model has recently been developed by Ohlmann and Siegel (2000). This enhanced model captures the rapid attenuation in the upper meter of the water column. For the present application, the shallowest point at which the flux is needed is typically 1 m, so the two-term expansion described above is sufficient.] Because the measurements were not made at exactly the same coordinates, we accounted for possible spatial variations by averaging profiles from days 365, 366, and 367, with double weight given to day 366. The result was $r_1 = 0.316; r_2 = 0.419; \mu_1 = 27.2\,\text{m}; \mu_2 = 2.93\,\text{m}$. By definition, $Tr(0) = 1 - \alpha$, where α is the albedo, here equal to 0.055 (Fairall et al. 1996). The fact that $r_1 + r_2 < 1 - \alpha$ indicates that significant radiation is absorbed between the surface and the uppermost measurement, located at $z = -0.5$ m (Ohlmann and Siegel 2000). Thus, we use Eq. (20) at all grid points except at the surface, where $Tr(0) = 0.945$.

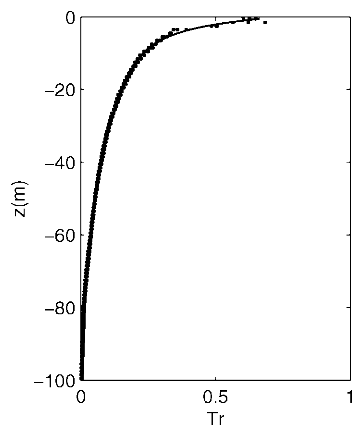

Fig. 2 Solar radiation transmissivity as a function of depth. *Dots* show daily averages from days 365, 366, and 367 as measured by Siegel et al. (1995). The *solid curve* represents the approximation (20), with parameter values as given in the text

4 Preliminary comparisons

The LES results for this period (Fig. 3b) are very similar to those described in Skyllingstad et al. (1999), although several minor upgrades have been made to the model in the interim (see Sect. 3.1). Momentum input from the wind is mixed through the upper ocean with only weak influence from the Coriolis force. Because no attempt has been made to include tidal effects or large-scale gradients in the LES model, the complex time dependence of the observed near-surface currents is not evident (cf. Figs. 1b and 3b, first and second frames). However, the nocturnal upper ocean exhibits a well-mixed velocity structure consistent with the observations. The modeled thermal evolution is quite similar to observations, although there is slightly more daytime heating and less night-time cooling. This discrepancy is consistent with the slight advective cooling that emerged in the observational analyses of Smyth et al. (1996b) and Feng et al. (1998). Thermal stratification in the modeled nocturnal mixed layer is nearly neutral, as shown by the nearly vertical isotherms in frame 3 of Fig. 3b. Salinity (fourth frame of Fig. 3b) increases over most of the analysis period due to evaporation, though freshening due to rain is evident at $t = 2\,\text{h}$ and during the last few hours of the simulation. Like the temperature field, the nocturnal salinity field is well mixed near the surface, though it exhibits significant stratification between 50 and 60 m that is not evident in the temperature.

Figure 3c and 3d shows results from two versions of the KPP column model, initialized and forced in the same manner as the LES. The model used to generate Fig. 3c approximates turbulent fluxes in accordance with the original KPP rules of Large et al. (1994), while Fig. 3d corresponds to a revised version of the KPP to be described later in this paper. To motivate the latter, we now compare the results of the original KPP model (Fig. 3c) with the LES (Fig. 3b). Three important differences are evident.

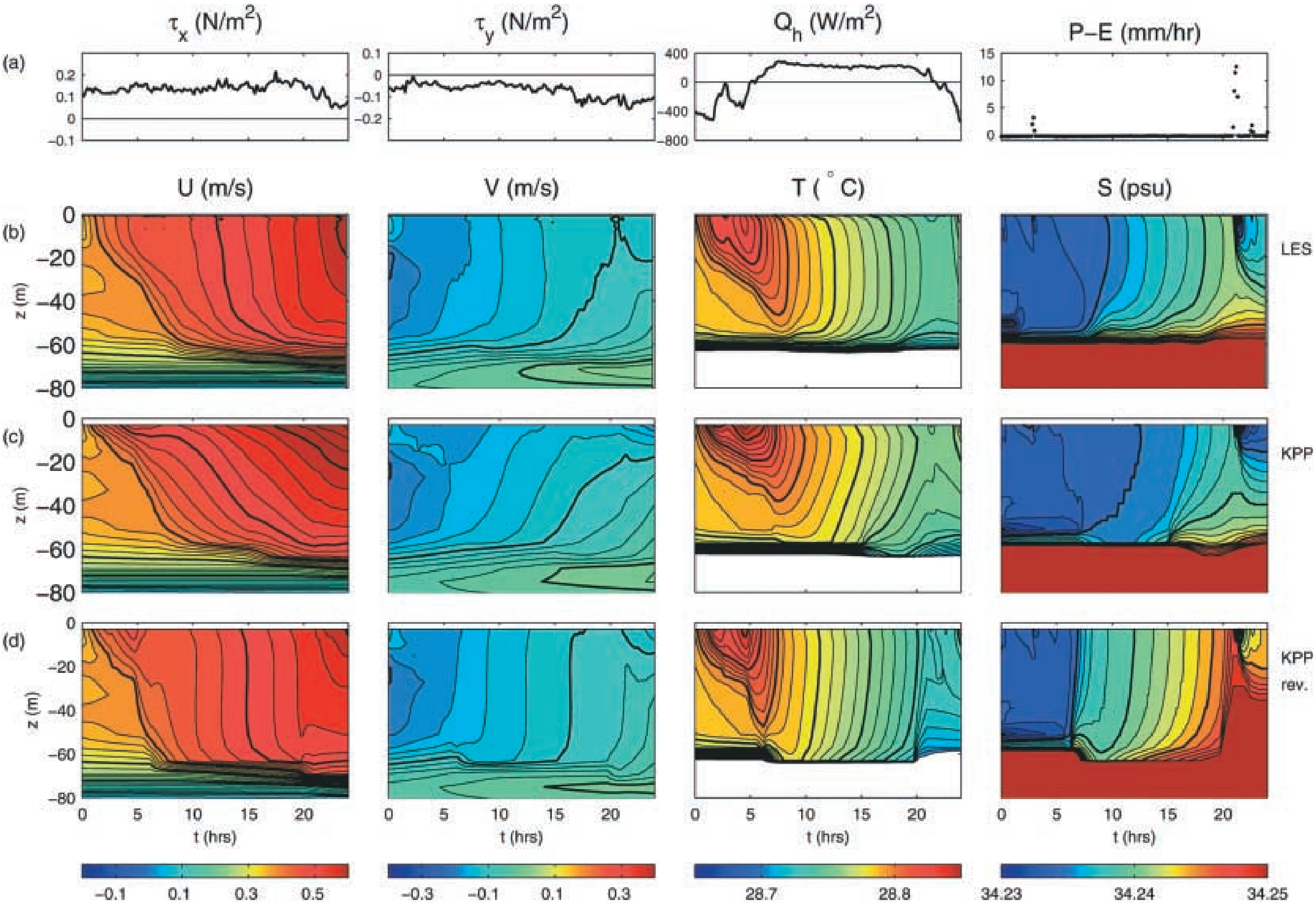

Fig. 3a–d Model results. **a** Wind stresses, net surface heat flux, and net precipitation rate observed at 156 E, −1.75 S for the 24-h period beginning on day 366 of 1992. **b, c, d** Time–depth sections of zonal current, meridional current, temperature, and salinity. **b** LES; **c** original KPP; **d** revised KPP

1. Most obviously, both velocity components exhibit significant gradients within the nocturnal mixed layer in the KPP case, as do the temperature and the salinity. The temperature gradient in this regime is not only nonzero but positive, opposite to the observed gradient (cf. Figs. 3c and 1b, third frame).
2. Upper-ocean heating during the first few hours of the simulation is much more pronounced in the KPP case than in the LES.
3. Near-surface shear is stronger in the KPP than in the LES throughout the simulation period.

In Sect. 5, we will describe these discrepancies quantitatively and seek to reduce them via revisions to the KPP model. We will use the LES results as a standard against which to test and calibrate our revisions. Our confidence in the LES as the appropriate "ground truth" for this exercise is based on several factors. First, while the LES does not contain the entirety of upper ocean physics, it contains that part which the KPP attempts to model, namely vertical fluxes due to turbulence, and it represents the large turbulent eddies that drive those fluxes explicitly. This particular LES model has been tested via comparison with microstructure measurements, and has been found to reproduce the observed statistics of turbulence extremely well within well-established limits (Skyllingstad et al. 1999). Finally, we can investigate the specific discrepancies between the KPP and the LES listed above while also considering the implications of the observational data for the veracity of the LES results. Like the LES, the observations show no sign of the strong gradients in U, V, T, and S developed by the KPP in the interior of the nocturnal mixed layer (Fig. 1b). Daytime heating is even weaker in the observations than in the LES, though this difference is exaggerated by advective cooling. Finally, the observations show no evidence of the strong shears developed by the KPP in the upper few meters, though this could also be due to observational uncertainties. Although these comparisons are not conclusive, the weight of evidence suggests that the LES results provide a reasonable standard against which to test the KPP model.

5 Modifications to the KPP

After considerable experimentation, we have identified several modifications to the KPP that appear to be of general utility. In this section, we describe these revisions in roughly the chronological order in which they become important in the present simulations. We begin with enhanced mixing due to Langmuir cells, which modulates near-surface warming during the first 6 h of the simulation period. We then describe the nonlocal fluxes of momentum and scalars, which determine vertical gradients in the nocturnal mixed layer. Finally, we show that unrealistically strong shears in the upper few meters may be controlled by including shear due to the Stokes drift in the momentum mixing term.

5.1 Amplification of wind-driven mixing by Langmuir cells

The moderate daytime warming in the LES is largely a result of Langmuir cells, which distribute solar heat over the upper few tens of meters. This effect is missing from the existing KPP model, with the result that upper ocean temperatures (averaged over the uppermost 10 m) increased by 0.02 °C more in the KPP than in the LES (Fig. 4, solid curves). Attempts to produce sufficient near-surface mixing in the KPP by varying the values of existing parameters by reasonable amounts have not been successful.

McWilliams and Sullivan (2001) suggest a parameterization in terms of Langmuir number (see Sect. 3.2), which effectively boosts the turbulent velocity scales w_m and w_s by about a factor of 3 for the present case. This leads to reduced daytime warming near the surface, in qualitative agreement with LES (Fig. 4, asterisks). However, the reduction in daytime warming is insufficient to reproduce the LES results quantitatively, while application of the parameterization during nocturnal convection causes unrealistically rapid mixing throughout the mixed layer.

The Langmuir cell parameterization shown in Fig. 4 was calibrated for weakly stable conditions. Evidently, the scheme mixes too weakly under strongly stable conditions ($0 < t < 6$ h) and too strongly under unstable conditions. We therefore make the amplitude parameter C_w a function of stability using Eq. (13). We now have two free parameters, C_{wo} and l, to calibrate. McWilliams and Sullivan results provide one data point, which we fit to Eq. (13) to infer the relation $C_{wo} = 0.08/0.726^l$. Figure 5 shows upper-ocean warming for two additional choices of C_{wo} and l that obey this relation, and one that does not (along with the original KPP and "target" LES results).

The choice $C_{wo} = 0.15, l = 2$ (dashed curve on Fig. 5) provides a much improved fit to the LES, although it mixes too weakly (i.e., allows too much heating in the upper 10 m) throughout the simulation. More extreme stability dependence is provided by the case $C_{wo} = 0.29$, $l = 4$ (dots, Fig. 5). In this case, the Langmuir cell effect ceases abruptly as the surface fluxes become stable. The result is reduced near-surface mixing in the early evening. The final case shown is $C_{wo} = 0.29, l = 2$ (circles, Fig. 5), which provides the best overall fit to our LES results. However, this is the case that does not obey the constraint $C_{wo} = 0.08/0.726^l$, i.e., it would not provide a good fit to the McWilliams and Sullivan results.

For the remaining analyses, we make the conservative choice $C_{wo} = 0.15, l = 2$. This choice provides enough extra mixing under stable conditions to greatly ameliorate the problem of excessive daytime heating, does not lead to excessive mixing at night, and reproduces the McWilliams and Sullivan (2001) result $C_w = 0.08$ for the appropriate values of u_* and w_*.

5.2 Nonlocal momentum flux

The amplitude parameter C_m^* for the nonlocal momentum flux has been set to zero in previous versions of the KPP rules. Here, we assign a nonzero value

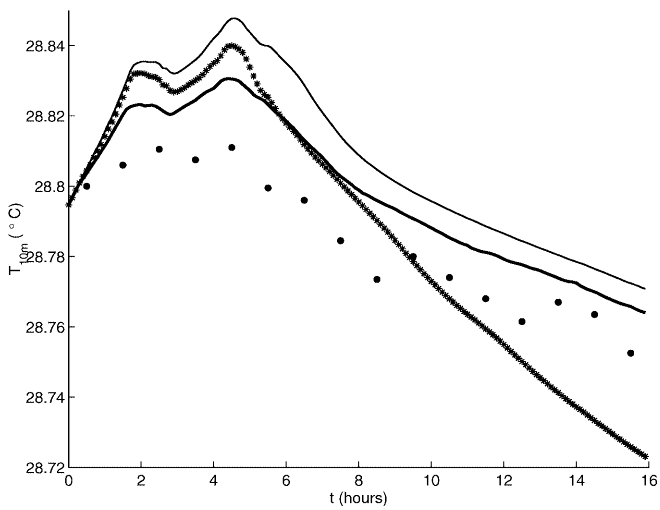

Fig. 4 Temperature averaged over the upper 10 m. *Dots* Observations; *thick curve* LES; *thin curve* original KPP, *asterisks* KPP with McWilliams and Sullivan (2001) parameterization of mixing due to Langmuir cells ($C_{wo} = 0.08, l = 0$)

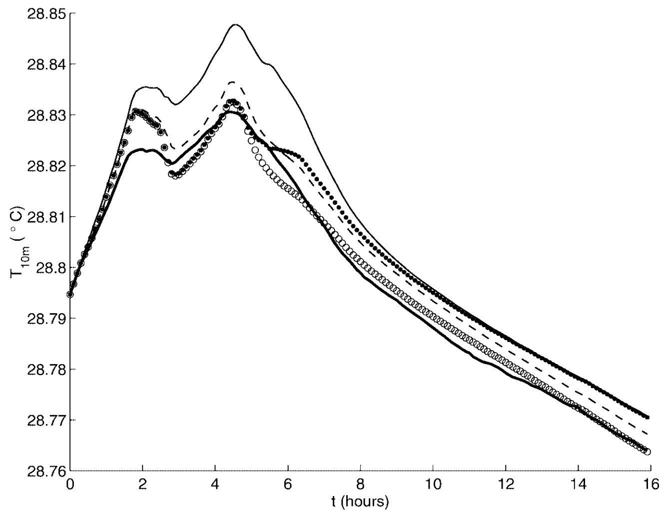

Fig. 5 Temperature averaged over the upper 10 m. *Thick curve* LES; *thin curve* original KPP; *dashed curve* KPP with MS parameterization of mixing due to Langmuir cells, but $C_{wo} = 0.15, l = 2$; *dotted curve* $C_{wo} = 0.29, l = 4$. *circles* $C_{wo} = 0.29, l = 2$

to that parameter in order to reduce the shear in the nocturnal mixed layer from the large value seen in Fig. 3c to a level more consistent with the LES and observed values.

To make this comparison quantitative, we compute the arithmetic mean of the zonal shear $\partial U/\partial z$ in the regime -40 m $< z < -20$ m; 11 h $< t <$ 20 h, which represents the interior of the nocturnal mixed layer. Also of interest is the zonal acceleration over the same depth–time range. These parameters are shown as functions of C_m^* in Fig. 6. As anticipated, the mean shear decreases as C_m^* increases from zero (Fig. 6a), and reaches zero when $C_m^* = 5.2$. The LES mean shear is best reproduced using the value $C_m^* = 3.3$. The optimal value of Brown and Grant (1997), $C_m^* = 2.3$, yields a mean shear part way between the LES value and the observed value. For the remaining analyses, we choose the intermediate value $C_m^* = 3.0$.

The acceleration is slightly greater than the LES value (Fig. 6b), and does not vary significantly with C_m^*. Also shown in Fig. 6 are results for a new set of values for the parameters C_s^* and C_v, whose derivation is described in the next subsection. Note for now that these revised values for C_s^* and C_v have a minimal effect on the zonal shear and acceleration in the nocturnal boundary layer, and therefore do not affect the optimal choice of C_m.

Figure 7 shows profiles of the vertical flux of zonal momentum in the nocturnal boundary layer. Flux profiles are averaged over a 9-h period during which mixed-layer depth was nearly stationary and vigorous convective turbulence was driven by surface cooling. In the original KPP (Fig. 7b), the flux is entirely local and is slightly stronger than in the LES results (Fig. 7a). In the revised KPP case, the net flux is nearly identical to that found in the original KPP, but that flux is now composed of local and nonlocal components whose overall magnitude is comparable.

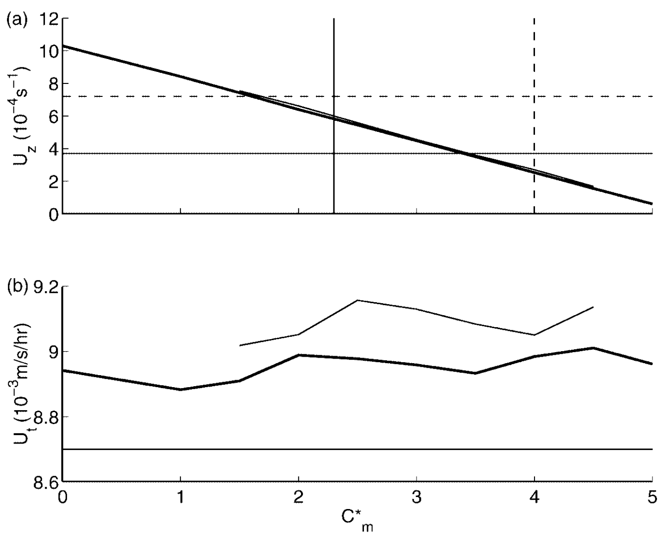

Fig. 6a, b Zonal shear and acceleration, averaged over $-40\,\text{m} < z < -20\,\text{m}$; $11\,\text{h} < t < 20\,\text{h}$, as functions of the nonlocal momentum flux amplitude parameter C_m^*. *Thick curve* $C_s^* = 10, C_v = 1.5$ (original KPP values); *thin curve* $C_s^* = 5, C_v = 1.0$ (revised values discussed in Section 5.3). **a** Shear. *Horizontal lines*: solid LES shear; *dashed* observed shear; *vertical lines* indicate values derived by Brown and Grant (1997) from atmospheric simulations: *solid* optimal value; *dashed* maximum value. **b** Acceleration. *Horizontal line* LES acceleration. (Observed acceleration is not shown because it is dominated by tides)

5.3 Nonlocal scalar fluxes

The amplitude parameter C_s^* for the nonlocal scalar flux has been set to 10 in previous versions of the KPP rules, based on the original estimates of Deardorff (1972) and the simulations of Mailhot and Benoit (1982). Calibrations by Therry and Lacarrere (1983) and Holtzag and Moeng (1991) have suggested the smaller value $C_s^* = 5$. In this subsection, we show that using the smaller value of C_s^* reduces the scalar gradients in the nocturnal mixed layer to more realistic values. However, the reduction of C_s^* necessitates compensating changes in other parameters.

Figure 8a shows the vertical temperature gradient averaged over the nocturnal mixed layer as a function of C_s^*. The LES value of the temperature gradient (horizontal line) is recovered when C_s^* is slightly greater than 4. Figure 8b shows β_T, the heat flux into the mixed layer due to entrainment at the mixed layer base, scaled by the surface heat flux. All versions of the KPP give values of β_T more negative than the LES result, indicating that the KPP develops a stronger entrainment flux. Correspondingly, the cooling rate in the nocturnal mixed layer (Fig. 8c) is slightly faster for the KPP cases than for the LES. This discrepancy is exacerbated by the reduction of C_s^* from its original value of 10.

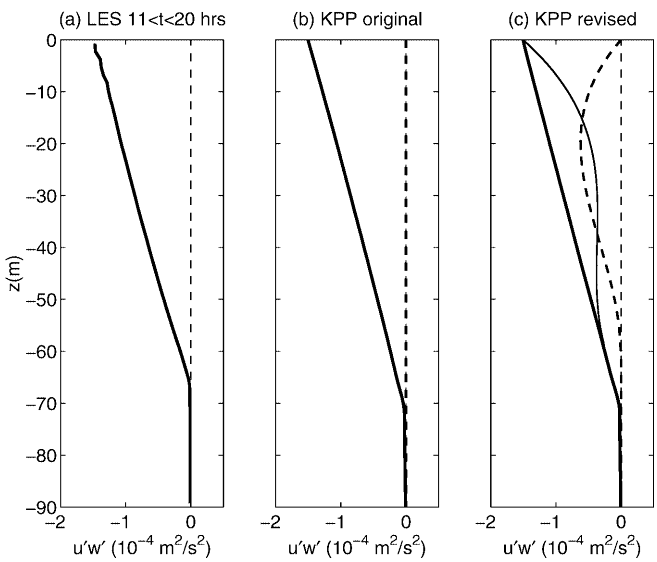

Fig. 7a–c Vertical flux of zonal momentum versus depth, averaged over $11\,\text{h} < t < 20\,\text{h}$. **a** LES. **b** Original KPP. **c** Revised KPP. *Thick solid curves* total flux; *thin solid curves* local flux; *thick dashed curves* nonlocal flux; *thin dashed lines* zero flux

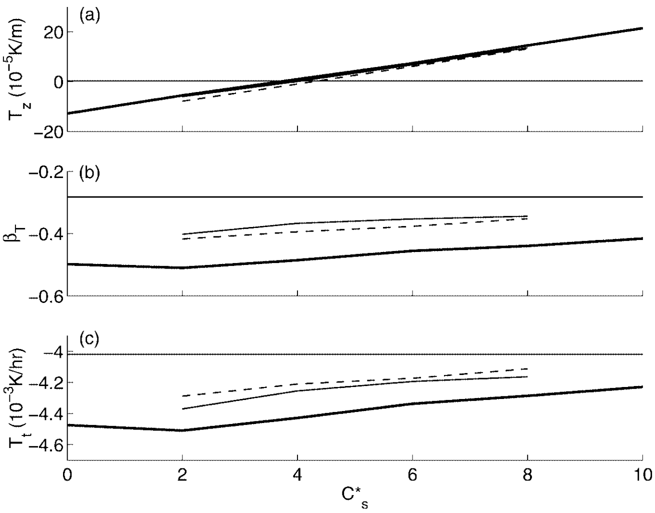

Fig. 8 a Vertical derivative of temperature, averaged over $-40\,\mathrm{m} < z < -20\,\mathrm{m}$; $11\,\mathrm{h} < t < 20\,\mathrm{h}$, as a function of the nonlocal scalar flux amplitude parameter C_s^*, with $C_m = 3$. **b** Ratio of the minimum (negative) heat flux in the entrainment zone to the (positive) surface heat flux, averaged over $11\,\mathrm{h} < t < 20\,\mathrm{h}$. **c** Time derivative of temperature, averaged over $-40\,\mathrm{m} < z < -20\,\mathrm{m}$; $11\,\mathrm{h} < t < 20\,\mathrm{h}$. *Thick curves* $\mathrm{Ri}_0 = 0.7, C_v = 1.5$ (original KPP values); *thin curves* $\mathrm{Ri}_o = 0.5, C_v = 1.5$; *dashed curves* $\mathrm{Ri}_0 = 0.7, C_v = 1.0$. *Solid horizontal lines* indicate the LES values

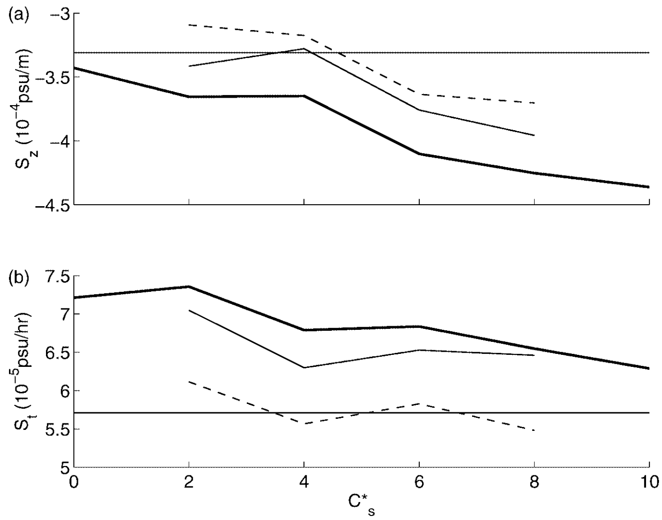

Fig. 9 a Vertical derivative of salinity, averaged over $-40\,\mathrm{m} < z < -20\,\mathrm{m}$; $11\,\mathrm{h} < t < 20\,\mathrm{h}$, as a function of the nonlocal scalar flux amplitude parameter C_s^*, with $C_m = 3$. **b** Time derivative of salinity, averaged over the same regime. *Thick curves* $\mathrm{Ri}_0 = 0.7$, $C_v = 1.5$ (original KPP values); *thin curves* $\mathrm{Ri}_0 = 0.5, C_v = 1.5$; *dashed curves* $\mathrm{Ri}_0 = 0.7, C_v = 1.0$. *Horizontal lines* indicate the LES values

Our intent now is to identify other parameters whose values may be altered in order to remove this undesirable increase in entrainment due to the reduction in the nonlocal scalar fluxes. We do not attempt to match the LES results in this respect; our goal is only to recover the smaller mismatch delivered by the original KPP parameter values. After some experimentation, we have found two reasonable candidate parameters. The first is Ri_0, the cutoff value for the Richardson number in the parameterization Eq. (8) of turbulence below the boundary layer. The result of reducing Ri_0 from its original value of 0.7 to 0.5 is shown by the thin solid curves in Fig. 8. The second possibility is to reduce the value of C_v, effectively reducing the turbulent velocity parameter V_t that appears in the bulk Richardson number used to determine boundary layer depth. The results of reducing C_v from 1.5 to 1.0 are shown by the dashed curves in Fig. 8. The values of Ri_0 and C_v have little effect on the mean temperature gradients shown in Fig. 8a. However, both of these changes compensate effectively for the reduction in the value of C_s^*, reducing the rate of entrainment into the mixed layer to below the value found in the original KPP (though the entrainment rate remains higher than in the LES results).

Similar results are found via analysis of the salinity field (Fig. 9). Reduction of C_s^* from 10 reduces the vertical salinity gradient in the nocturnal mixed layer from the unrealistically large value delivered by the original KPP to a smaller value consistent with the LES results (Fig. 9a). As with temperature, this change results in increased entrainment at the mixed layer base, and thus in a more rapid increase in mixed-layer salinity (Fig. 9b). Setting Ri_0 to 0.5 reduces salt entrainment nearly to the rate delivered by the original KPP (the value of the thick, solid curve at $C_s^* = 10$), while reduction of C_v to 1.0 reduces entrainment to a rate consistent with the LES results (horizontal solid line).

Results presented so far give no compelling reason to choose between Ri_0 and C_v as the parameter whose value should be reduced to compensate for the reduced nonlocal scalar flux. Reducing Ri_0 acts to reduce mixing rates below the boundary layer, whereas reducing C_v tends to make the boundary layer slightly shallower. Since the boundary layer generated by the KPP is already too deep (Fig. 7), we choose the second alternative. For the remainder of this discussion, we will set C_s to 5.0 and C_v to 1.0, leaving Ri_0 at its original value 0.7.

Our changes to the values of C_s^* and C_v raise the possibility that the optimal value for C_m^* calculated in Section 5.2 is no longer optimal. This turns out not to be the case. Results shown in Fig. 6 change only slightly when the revised values of C_s^* and C_v are employed (thin, solid curves on Fig. 6), and the arguments for our choice $C_m^* = 3$ are unaffected.

5.4 Mixing of the Stokes drift velocity profile

As noted in Section 4, the KPP tends to produce strong near-surface shears relative to LES. In the LES, these shears are prevented by strong, small-scale Langmuir cells in the upper few meters. The corresponding mixing can be achieved in the KPP by adding strong momentum mixing near the surface. McWilliams and Sullivan (2001) suggest that the effective velocity gradient that controls the nonlocal momentum flux be supplemented with the shear of the Stokes drift current. The latter is given by

$$\vec{u}_s(z) = U_s e^{\mu z} \hat{\boldsymbol{e}} \tag{21}$$

where U_s is the maximum Stokes drift velocity, determined by wave height and equal to 11.5 u_* in the present LES. The unit vector $\hat{\mathbf{e}}$ points in the direction of the wind, and the vertical decay rate μ is equal to $2\pi/\lambda$, where λ is the dominant wavelength of the surface wave field, here equal to 30 m.

Figure 10 shows the zonal and meridional velocity components, averaged over the analysis period. Cases shown include the LES along with the KPP with $\partial\vec{u}_s/\partial z$ added to $\partial\vec{U}/\partial z$ in the parameterization (Eq. 7) of the vertical momentum flux in various proportions (quantified by C_{St}). The LES velocity profiles (thick curves on Fig. 10) exhibit very little shear in the upper 10 m. In contrast, the original KPP profiles (thin curves) are strongly sheared. When revised to take account of amplified mixing due to Langmuir cells (Sect. 5.1), nonlocal momentum fluxes (Sect. 5.2), and reduced nonlocal scalar fluxes compensated by reduction of C_v (Sect. 5.3), the KPP model exhibits strong shear only in the upper 5 m (dots on Fig. 10). When the shear of the Stokes drift is added to the nonlocal momentum flux as described above, shear is reduced further, to the point of slight overcompensation (plus signs on Fig. 10). The asterisks on Fig. 10 show an intermediate case in which 70% of the Stokes drift shear has been added to the nonlocal flux. This provides the best match to the LES velocity profile.

Complete fields delivered by this model are shown in Fig. 3d. Vertical gradients of the velocity, temperature, and salinity in the nocturnal mixed layer now correspond well with LES results (Fig. 3b), in contrast with the original KPP results (Fig. 3c). Solar heating during the first few hours of the simulation now agrees with the LES results, and the anomalous current shears that the original KPP developed in the upper 10 m have been effectively removed.

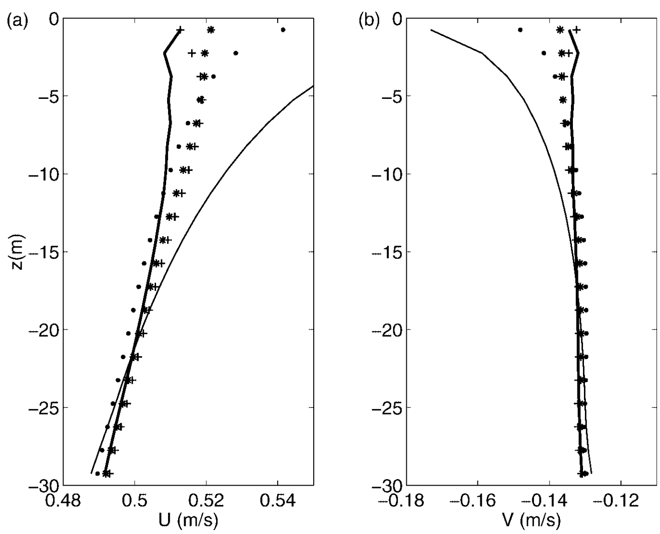

Fig. 10 Zonal (**a**) and meridional (**b**) velocity components in the upper 30 m, averaged over the 24-h run. *Thick*, solid curve LES; *thin, solid curve* original KPP; *dots* KPP with $C_{St} = 0$; *plus signs* KPP with $C_{St} = 1$; *asterisks* KPP with $C_{St} = 0.7$

6 Conclusions

We have tested and revised the KPP model using observations and LES of the upper equatorial Pacific during a westerly windburst. Four revisions have been made to the existing KPP:

1. The turbulent velocity scales have been amplified to account for mixing by Langmuir cells using Eq. (12). The effect is reduced during unstable conditions using Eq. (13), with $C_{wo} = 0.15$ and $l = 2$. These parameter values were arrived at by requiring that daytime solar heat input be mixed at a rate consistent with LES, and are consistent with the parameterization suggested by McWilliams and Sullivan (2001).
2. A nonlocal momentum flux was added in accordance with Eq. (16). Stability dependence was provided using Eq. (18), and the flux was directed parallel to the wind. The amplitude parameter C_m^* was set to 3.0 by requiring that the mean zonal shear in the nocturnal mixed layer match the LES value.
3. The amplitude parameter for the nonlocal scalar flux was reduced from its original value $C_s^* = 10$ to $C_s^* = 5$ in order to obtain realistic scalar gradients in the nocturnal mixed layer. To compensate for excessive entrainment at the base of the mixed layer due to this change in C_s^*, we reduced the turbulent velocity parameter C_v to 1.0 from its original value 1.5.
4. Strong, near-surface shears appearing in the KPP results were removed by adding 0.7 times the shear of the Stokes drift current to the effective shear governing the nonlocal momentum flux.

The fourth change listed above is somewhat ad hoc; there is no particular reason why the shear of the Stokes drift should contribute to the momentum flux in this way. This artifice merely provides enhanced mixing near the surface with the correct properties to remove the strong near-surface shear developed by the KPP as a result of matching to a surface-layer similarity solution (Large et al. 1994). Such matching is probably inappropriate in the ocean due to the presence of surface waves. A more physical solution to this problem must await further progress in the parameterization of surface-wave effects.

These changes led to much better agreement between the KPP results and the corresponding LES. By generating realistically small gradients in the nocturnal mixed layer, these changes will improve the representation of lateral advection in large-scale models that use KPP to model vertical mixing. Finally, increased mixing of solar heat will improve predictions of sea-surface temperature, a crucial factor in coupled models.

Further development of the KPP rules will require testing against a wider range of observational datasets. Such tests must examine the generality of the nonlocal flux and Langmuir cell parameterizations used here. In particular, further testing must address three issues that have not been adequately resolved in the present work:

- The optimal choice of the direction vector $\hat{e}$ for the nonlocal momentum flux should be identifiable in midlatitude regimes where surface currents are less likely to be aligned with the wind.
- Unwanted effects of reducing the value of the nonlocal scalar flux parameter C_s^* from 10 to 5 may be removed by reducing either C_v and Ri_0 (or some combination of the two). Detailed examination of mixing around the base of the boundary layer will allow us to make that choice with more confidence.
- Accounting for fluxes due to breaking surface waves remains a central goal in modeling upper-ocean turbulence.

Acknowledgements Optical transmissivity data were generously provided by Dave Siegel and Carter Ohlmann. Supercomputer time for the LES computations was provided by the National Center for Atmospheric Research. The research was funded by the National Science Foundation under grant OCE9711862.

References

Anis A, Moum J (1992) The superadiabatic surface layer of the ocean during convection. J Phys Oceanogr 22: 1221–1227

Brown A, Grant A (1997) Non-local mixing of momentum in the convective boundary layer. Boundary Layer Meteorol 84: 1–22

Burchard H, Petersen O, Rippeth T (1998) Comparing the performance of the Mellor–Yamada and the k–ϵ two-equation turbulence models. J Geophys Res 103: 10543–10554

Deardorff J (1972) Theoretical expression for the countergradient vertical heat flux. J Geophys Res 77: 5900–5904

Ducros F, Comte P, Lesieur M (1996) Large eddy simulation of transition to turbulence in a boundary layer developing spatially over a flat plate. J Fluid Mech 326: 1–36

Fairall C, Bradley E, Rogers D, Edson J, Young G (1996) The TOGA-COARE bulk flux algorithm. J Geophys Res 101: 3747–3764

Feng M, Hacker P, Lukas R (1998) Upper-ocean heat and salt balances in response to a westerly wind burst in the western equatorial Pacific during TOGA-COARE. J Geophys Res 103: 10289–10311

Frech M, Mahrt L (1995) A two-scale mixing formulation for the atmospheric boundary layer. Boundary Layer Meteorology 73: 91–104

Holtzag A, Moeng C.-H (1991) Eddy diffusivity and countergradient transport in the convective atmospheric boundary layer. J Atmos Sci 48: 1690–1698

Kantha L, Clayson C (1994) An improved mixed layer model for geophysical applications. J Geophys Res 99: 25235–25266

Large W, Gent P (1999) Validation of vertical mixing in an equatorial ocean model using large eddy simulations and observations. J Phys Oceanogr 29: 449–464

Large W, McWilliams J, Doney S (1994) Ocean vertical mixing: a review and a model with a nonlocal boundary layer parameterization. Rev Geophys 32(4): 363–403

Mailhot J, Benoit R (1982) A finite-element model of the atmospheric boundary layer suitable for use with numerical weather prediction models. J Atmos Sci 39: 2249–2262

McWilliams J, Sullivan P (2001) Vertical mixing by Langmuir circulations. Spill Sci Technol Bull 6: 225–237

Mellor G, Yamada T (1982) Development of a turbulence closure model for geophysical fluid problems. Rev Geophys Space Phys 20: 851–875

Moum J, Caldwell D (1994) Experiment explores the dynamics of ocean mixing. EOS Trans 75: 489–495

Moum JN, Gregg MC, Lien RC, Carr ME (1995) Comparison of turbulence kinetic energy dissipation rate estimates from two ocean microstructure profilers. J Atmos Oceanic Technol 12(2): 346–366

Ohlmann J, Siegel D (2000) Ocean radiant heating, part 2: Parameterizing solar radiation transmission through the upper ocean. J Phys Oceanogr 30: 1849–1865

Ohlmann J, Siegel D, Washburn L (1998) Radiant heating of the western equatorial Pacific during TOGA-COARE. J Geophys Res 103: 5379–5395

Siegel D, Ohlmann J, Washburn L, Bidigare R, Nosse C, Fields E, Zhou Y (1995) Solar radiation, phytoplankton pigments, and the radiant heating of the equatorial Pacific Warm Pool. J Geophys Res 100: 4885–4891

Skyllingstad E, Smyth W, Moum J, Wijesekera H (1999) Turbulent dissipation during a westerly wind burst: a comparison of large eddy simulation results and microstructure measurements. J Phys Oceanogr 29: 5–29

Skyllingstad E, Smyth W, Crawford G (2000) Resonant wind-driven mixing in the ocean boundary layer. J Phys Oceanogr 30: 1866–1890

Smyth W, Hebert D, Moum J (1996a) Local ocean response to a multiphase westerly windburst, part 1: The dynamic response. J Geophys Res 101: 22495–22512

Smyth W, Hebert D, Moum J (1996b) Local ocean response to a multiphase westerly windburst, part 2: Thermal and freshwater responses. J Geophys Res 101: 22495–22512

Smyth W, Zavialov P, Moum J (1997) Decay of turbulence in the upper ocean following sudden isolation from surface forcing. J Phys Oceanogr 27: 810–822

Therry G, Lacarrere P (1983) Improving the eddy kinetic energy model for planetary boundary layer description. Boundary Layer Meteorol 25: 63–88

Troen I, Mahrt L (1986) A simple model of the atmospheric boundary layer; Sensitivity to surface evaporation. Boundary Layer Meteorol 37: 129–148

Webster P, Lukas R (1992) TOGA-COARE: the coupled ocean–atmosphere response experiment. Bull Am Met Soc 73: 1377–1415

Weller W, Anderson S (1996) Surface meteorology and air-sea fluxes in the western equatorial Pacific Warm Pool during the TOGA coupled ocean–atmosphere response experiment. J Climate 9: 1959–1991